Soft Matter

PAPER

View Article Online
View Journal | View Issue

Cite this: *Soft Matter*, 2019, **15**, 9244

The elastic Rayleigh drop

S. I. Tamim and J. B. Bostwick *

Received 29th August 2019,
Accepted 15th October 2019

DOI: 10.1039/c9sm01753d

rsc.li/soft-matter-journal

Bioprinting technologies rely on the formation of soft gel drops for printing tissue scaffolds and the dynamics of these drops can affect the process. A model is developed to describe the oscillations of a spherical gel drop with finite shear modulus, whose interface is held by surface tension. The governing elastodynamic equations are derived and a solution is constructed using displacement potentials decomposed into a spherical harmonic basis. The resulting nonlinear characteristic equation depends upon two dimensionless numbers, elastocapillary and compressibility, and admits two types of solutions, (i) spheroidal (or shape change) modes and (ii) torsional (rotational) modes. The torsional modes are unaffected by capillarity, whereas the frequency of shape oscillations depend upon both the elastocapillary and compressibility numbers. Two asymptotic dispersion relationships are derived and the limiting cases of the inviscid Rayleigh drop and elastic globe are recovered. For a fixed polar wavenumber, there exists an infinity of radial modes that each transition from an elasticity wave to a capillary wave upon increasing the elastocapillary number. At the transition, there is a qualitative change in the deformation field and a set of recirculation vortices develop at the free surface. Two special modes that concern volume oscillations and translational motion are characterized. A new instability is documented that reflects the balance between surface tension and compressibility effects due to the elasticity of the drop.

1 Introduction

More than a century ago, Lord Rayleigh[1] showed that an inviscid spherical drop held by surface tension σ will oscillate with characteristic frequency

$$\zeta^2 = l(l-1)(l+2), \tag{1}$$

and mode shape given by the spherical harmonic $Y_l^m(\theta,\varphi)$ with polar/azimtuhal $[l,m]$ wavenumber pair.[2] Here the frequency ζ is scaled by the capillary time scale $\sqrt{\rho R^3/\sigma}$, where σ, ρ, R are the liquid surface tension, density and drop radius, respectively. We call this the Rayleigh drop. The dispersion relationship (1) has seen widespread use in multiple technologies, such as spray cooling (drop atomization)[3] and inkjet printing (drop pinchoff).[4,5] Bioprinting applications, *e.g.* 3D printing of tissue scaffolds,[6,7] utilize the fluid mechanical principles of inkjet printing but adapted to biologically-compatible hydrogels, such as agarose and alginate.[8] These soft viscoelastic gels have a finite elasticity and often a complex rheology.[9,10] In this paper, we develop a theoretical model to predict the dispersion relationship for a soft spherical gel drop, which we refer to as the elastic Rayleigh drop.

Department of Mechanical Engineering, Clemson University, Clemson, SC 29634, USA. E-mail: jbostwi@clemson.edu

Soft gels are polymeric fluids, a sub-class of complex fluids, which are characterized by both a viscosity and elasticity. For capillary-driven flows, the dynamics are characterized by three relevant time scales; the polymer relaxation time $t_p = \lambda$, a viscous time scale $t_v = \gamma R/\sigma$ with γ the viscosity, and an inertial time scale $t_c = \sqrt{\rho R^3/\sigma}$.[11] Typical values for the rheological properties λ, γ are given in Barnes.[12] The relative balance of these time scales gives rise to dimensionless parameters that define the flow; the Ohnesorge number $\mathrm{Oh} \equiv t_v/t_c = \gamma/\sqrt{\rho\sigma R}$ balances viscosity and inertia, and the Deborah number $\mathrm{De} \equiv t_p/t_c = \lambda/\sqrt{\rho R^3/\sigma}$ balances the polymer relaxation with inertia. The special case $\mathrm{De} > 1 > \mathrm{Oh}$ ($t_p > t_c > t_v$) corresponds to an 'inviscid elastic fluid'[13] which is typical of dilute polymer concentrations, such as those typically used in bioinks. We are interested in this limiting case in which drop oscillations are affected by elasticity, capillarity and inertia.

Both surface tension and elasticity resist motion and that coupling defines an elastocapillary effect which becomes important on length scales smaller than the elastocapillary length $\ell_e \equiv \sigma/E$, where E is the elastic modulus. For a spherical gel drop, the relevant length scale is the drop radius R which allows one to define an elastocapillary number $\Sigma = \sigma/ER$. Note that bulk elastocapillarity is distinguished from bendocapillarity in which surface tension can bend a thin object with large elasticity. See the recent reviews by Style *et al.*,[14] Andreotti and Snoeijer,[15] Bico *et al.*[16] for a detailed discussion of the relevant

scaling arguments, and a summary of the many interesting recently observed and unexplained physics in this emerging field. We note that gels are typically viewed as solids and the existence of solid surface tension has been known for some time.[17] Pioneering experiments by Monroy and Langevin[18] were the first to observe elastocapillary waves on planar substrates and document the crossover between elastic and capillary waves. These results were shown to agree well with a theory developed by Harden *et al.*[19] In fact, many of the classical capillary-driven instabilities of fluid mechanics, *e.g.* Rayleigh–Taylor, Plateau–Rayleigh, have been observed in soft gels.[20–22] Chakrabarti and Chaudhury[23] have shown how the frequency response of sessile hydrogel drops is affected by elasticity. More recent work by Shao *et al.*[24] have shown the crossover from elastic to capillary waves on mechanically-excited Faraday waves on planar surfaces and used the observed dispersion relationship to estimate the solid surface tension. Our fundamental model of drop oscillations can be viewed as an extension of the Rayleigh drop which includes elastocapillary effects.

In general, gels exhibit frequency-dependent viscoelastic properties (or both solid- and fluid-like properties) which means our model could be framed from either a fluid dynamics or elasticity perspective. We note that the most commonly used biogel, agarose, behaves like a linear elastic solid over a large frequency range,[25] but some gels exhibit a nonlinear material response (*e.g.* strain stiffening).[26–29] However, we are interested in small amplitude oscillations in the linear elastic regime and nonlinear amplitude effects are outside the scope of this work. The duality between solid mechanics and fluid mechanics for our 'inviscid elastic fluid' means we could formulate the problem from either perspective. We adopt the solid mechanics perspective and assume our gel drop consists of a linear elastic material that is characterized by two Lamé parameters λ, μ and obeys the governing equations of linear elastodynamics.[30] Capillary effects enter the problem through the Young–Laplace equation on the free surface.[31–33] Elastic wave propagation on a sphere is qualitatively different from that on a plane; Rayleigh[34] waves on a semi-infinite half space are non-dispersive, whereas waves on a sphere are dispersive and have been observed over many different length scales, from geodynamics[35] and seismology[36] to nanophysics.[37,38] The invariance in wave dynamics over such a large length scale occurs because there is only one time scale for such problems, the elastic time scale $t_e = (\rho R^2/\mu)^{1/2}$. In our problem, we also have a capillary time scale $t_c = (\rho R^3/\sigma)^{1/2}$ and the balance between these two time scales gives rise to interesting dynamic elastocapillary effects.

We begin this paper by defining the elastodynamic equations that govern the motion of the spherical gel drop. Displacement potentials are introduced and we expand our solution in a spherical harmonic basis to generate a nonlinear characteristic equation for the scaled drop frequency, which depends upon elastocapillary and compressibility dimensionless numbers. Two mode types are reported; torsional modes have a non-deforming interface, while spheroidal modes are associated with shape change. Our solution recovers the limiting cases of the inviscid Rayleigh drop and the purely elastic globe. In the intermediate region between these two limits, we show there is a transition between elasticity-dominated and capillary-dominated motion and characterize the change in deformation field that occurs there. We identify two special motions, the 'breathing' and 'translational' modes, and characterize their dynamics. Our analysis of the breathing mode reveals a new fundamental instability that reflects a balance between surface tension and compressibility due to the elasticity of the drop. Lastly, some concluding remarks are offered.

2 Mathematical formulation

Consider the spherical gel drop of equilibrium radius R shown in Fig. 1. The interface is given a small perturbation ζ, which generates a time-dependent displacement field $\mathbf{U}(\mathbf{x},t)$ in the gel, which is assumed to be an isotropic, linear elastic material with density ρ, Lamé constants λ, μ, and surface tension σ. Normal modes $\mathbf{U}(\mathbf{x},t) = \mathbf{u}(\mathbf{x})e^{i\omega t}$ are assumed with ω the oscillation frequency. The displacement field is defined in the spherical coordinate system (r,θ,φ).

$$\mathbf{u} = u_r(r,\theta,\varphi)\hat{\boldsymbol{e}}_r + u_\theta(r,\theta,\varphi)\hat{\boldsymbol{e}}_\theta + u_\varphi(r,\theta,\varphi)\hat{\boldsymbol{e}}_\varphi. \tag{2}$$

2.1 Field equations

The displacement field $\mathbf{u}$ is governed by the elastodynamic Navier equations,

$$(\lambda + \mu)\nabla(\nabla\cdot\mathbf{u}) + \mu\nabla^2\mathbf{u} = -\rho\omega^2\mathbf{u}. \tag{3}$$

For this linear elastic material, the strain field is given by $\boldsymbol{\varepsilon} = (\nabla\mathbf{u} + \nabla\mathbf{u}^T)/2$ and the stress field by $\tau_{ij} = \lambda\varepsilon_{kk}\delta_{ij} + 2\mu\varepsilon_{ij}$.

Continuity of stress on the free surface $r = R$ requires

$$\tau_{rr} = \frac{\sigma}{R^2}\left(\nabla_\parallel{}^2 u_r + 2u_r\right),\ \tau_{r\theta} = 0,\ \tau_{r\varphi} = 0, \tag{4}$$

where

$$\nabla_\parallel{}^2 \equiv \frac{1}{\sin\theta}\frac{\partial}{\partial\theta}\left(\sin\theta\frac{\partial}{\partial\theta}\right) + \frac{1}{\sin^2\theta}\frac{\partial^2}{\partial\varphi} \tag{5}$$

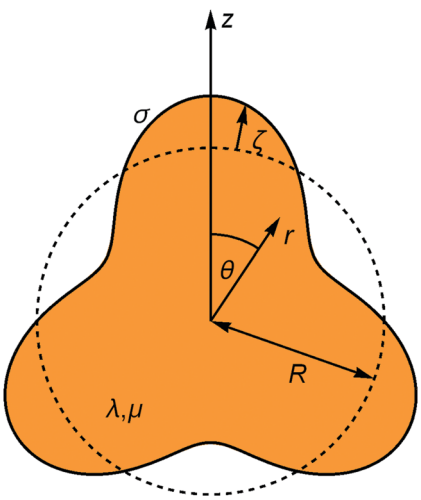

Fig. 1 Definition sketch of the spherical gel drop.

is the surface Laplacian. The normal stress condition in eqn (4) is simply the linearized Young–Laplace equation relating the jump in normal stress across the free surface to the mean curvature there.

2.2 Displacement potential

The governing eqn (3) is simplified by defining the displacement field $\mathbf{u}$ in terms of the scalar potentials Φ, T, S;

$$\mathbf{u} = \nabla\Phi + \nabla\times(T\hat{\boldsymbol{e}}_r) + \nabla\times\nabla\times(S\hat{\boldsymbol{e}}_r). \tag{6}$$

Substituting (6) into (3) yields a set of uncoupled Helmholtz equations for the potentials,

$$\begin{aligned}&\nabla^2\Phi + \alpha^2\Phi = 0,\ \nabla^2\left(\frac{T}{r}\right) + \beta^2\left(\frac{T}{r}\right) = 0,\\ &\nabla^2\left(\frac{S}{r}\right) + \beta^2\left(\frac{S}{r}\right) = 0,\end{aligned} \tag{7}$$

with $\alpha \equiv \omega\sqrt{\frac{\rho}{\lambda+2\mu}}$ and $\beta \equiv \omega\sqrt{\frac{\rho}{\mu}}$. Eqn (7) yields compressional and shear wave solutions with velocities $c_p = \sqrt{\frac{\lambda+2\mu}{\rho}}$ and $c_s = \sqrt{\frac{\mu}{\rho}}$, respectively.[39]

The general solution of (7) can be written by expanding the potentials Φ, T, S in a spherical harmonic $Y_l^m(\theta,\varphi)$ basis;[40]

$$\begin{aligned}\Phi &= \sum_{l=0}^{\infty}\sum_{m=-l}^{l} A_{lm} j_l(\alpha r) Y_l^m(\theta,\varphi),\\ T &= \sum_{l=0}^{\infty}\sum_{m=-l}^{l} rB_{lm} j_l(\beta r) Y_l^m(\theta,\varphi),\\ S &= \sum_{l=0}^{\infty}\sum_{m=-l}^{l} rC_{lm} j_l(\beta r) Y_l^m(\theta,\varphi),\end{aligned} \tag{8}$$

where j_l is the spherical Bessel functions of the first kind. Note that we suppress the spherical Bessel function of the second kind in our solution, because they diverge at the origin and are unphysical. The unknown constants A_{lm}, B_{lm}, C_{lm} are determined from the boundary conditions (4). For reference, the components of the displacement field (u_r, u_θ, u_φ) are expressed with respect to these unknown constants in Appendix A.

2.3 Characteristic equation

We scale lengths by R, time with the elastic shear wave time scale $\sqrt{\rho R^2/\mu}$, and apply the solution (8) to (4) to yield a set of linear equations,

$$\begin{aligned}&A_{lm}T_{11}(\kappa\eta) + C_{lm}T_{31}(\eta)\\ &\quad= \frac{\Sigma}{2}(2-l-l^2)(A_{lm}Q_1(\kappa\eta) + C_{lm}Q_2(\eta))\end{aligned} \tag{9a}$$

$$A_{lm}T_{12}(\kappa\eta) + C_{lm}T_{32}(\eta) = 0 \tag{9b}$$

$$B_{lm}T_{22}(\eta) = 0, \tag{9c}$$

for the dimensionless frequency $\eta \equiv \omega R\sqrt{\rho/\mu}$. Here

$$\begin{aligned}T_{11} &= \left(l^2 - l - \frac{1}{2}\eta^2\right)j_l(\kappa\eta) + 2\kappa\eta j_{l+1}(\kappa\eta),\\ T_{12} &= (l-1)j_l(\kappa\eta) - \kappa\eta j_{l+1}(\kappa\eta),\\ T_{22} &= (l-1)j_l(\eta) - \eta j_{l+1}(\eta),\\ T_{31} &= l(l+1)\{(l-1)j_l(\eta) - \eta j_{l+1}(\eta)\},\\ T_{32} &= \left(l^2 - 1 - \frac{1}{2}\eta^2\right)j_l(\eta) + \eta j_{l+1}(\eta),\\ Q_1 &= lj_l(\kappa\eta) - \kappa\eta j_{l+1}(\kappa\eta),\ Q_2 = l(l+1)j_l(\eta).\end{aligned} \tag{10}$$

Two dimensionless groups result from this choice of scaling,

$$\kappa \equiv \frac{\alpha}{\beta} = \sqrt{\frac{\mu}{\lambda+2\mu}},\quad \Sigma \equiv \frac{\sigma}{\mu R}, \tag{11}$$

where the compressibility number κ is the ratio of compressional to shear wave speeds and the elastocapillary number Σ measures the relative importance of surface tension and elasticity.

Eqn (9) admits two sets of solutions, which we will refer to as torsional and spheroidal modes. Eqn (9c) is uncoupled and gives the characteristic equation for the torsional modes,

$$(l-1)j_l(\eta) - \eta j_{l+1}(\eta) = 0, \tag{12}$$

which is consistent with Lamb's modal classification.[41] The spheroidal modes satisfy the set of equations

$$\begin{aligned}&T_{12}(\kappa\eta)A_{lm} + T_{32}(\eta)C_{lm} = 0,\\ &\left(T_{11}(\kappa\eta) - \frac{\Sigma}{2}(2-l-l^2)Q_1(\kappa\eta)\right)A_{lm}\\ &+ \left(T_{31}(\eta) - \frac{\Sigma}{2}(2-l-l^2)Q_2(\eta)\right)C_{lm} = 0.\end{aligned} \tag{13}$$

The solvability condition generates the nonlinear characteristic equation,

$$\begin{aligned}&-\frac{1}{2}\left(\frac{2l^2-l-1}{\eta^2} - \frac{1}{2}\right)j_l(\kappa\eta)j_l(\eta)\\ &+ \left(\frac{l^3+l^2-2l}{\eta^3} - \frac{1}{2\eta}\right)j_l(\kappa\eta)j_{l+1}(\eta)\\ &+ \left(\frac{l^3+2l^2-l-2}{\eta^3} - \frac{1}{\eta}\right)\kappa j_l(\kappa\eta)j_{l+1}(\eta)\\ &+ \frac{2-l-l^2}{\eta^2}\kappa j_{l+1}(\kappa\eta)j_l(\kappa\eta)\\ &- \frac{\Sigma}{2}(2-l-l^2)\left(-\frac{l}{2\eta^2}j_l(\kappa\eta)j_l(\eta) + \frac{l}{\eta^3}j_l(\kappa\eta)j_{l+1}(\eta)\right.\\ &- \left(\frac{2l^2-l-1}{\eta^3} - \frac{1}{2\eta}\right)\kappa j_{l+1}(\kappa\eta)j_l(\eta)\\ &\left.-\frac{\kappa}{\eta^2}j_{l+1}(\kappa\eta)j_{l+1}(\eta)\right) = 0,\end{aligned} \tag{14}$$

for the frequency η of the spheroidal modes. These solutions correspond to the shape oscillations of the drop. There are an infinite number of roots η to eqn (14), which depend upon the parameters Σ, l, κ. We enumerate these solutions using the radial mode number s that corresponds to the sth root of the characteristic eqn (14). To summarize, we report $\eta = \eta(s, l, \Sigma, \kappa)$. The absence of the wavenumber m implies the frequency spectrum is degenerate with respect to m, as with the inviscid Rayleigh drop.[42] For $\Sigma = 0$, surface tension effects are negligible and we recover the characteristic equation for an elastic globe.[30]

2.4 Incompressible limit $\kappa \to 0$

Elastic materials typically have a finite compressibility, but many soft gels of interest are often incompressible.[43,44] The characteristic eqn (14) can be greatly simplified in this limit. To illustrate, we redefine κ with respect to the Poisson ratio ν, $\kappa \equiv \sqrt{\frac{1-2\nu}{2(1-\nu)}}$. For incompressible materials $\nu = 1/2$, $\kappa \to 0$ and the resulting characteristic equation is

$$\eta\left(2+\eta^2-l^3\Sigma+2l(\Sigma+1)-l^2(\Sigma+4)\right)j_l(\eta) - 2\left(\eta^2+l(\Sigma+2)(2-l-l^2)\right)j_{l+1}(\eta) = 0. \quad (15)$$

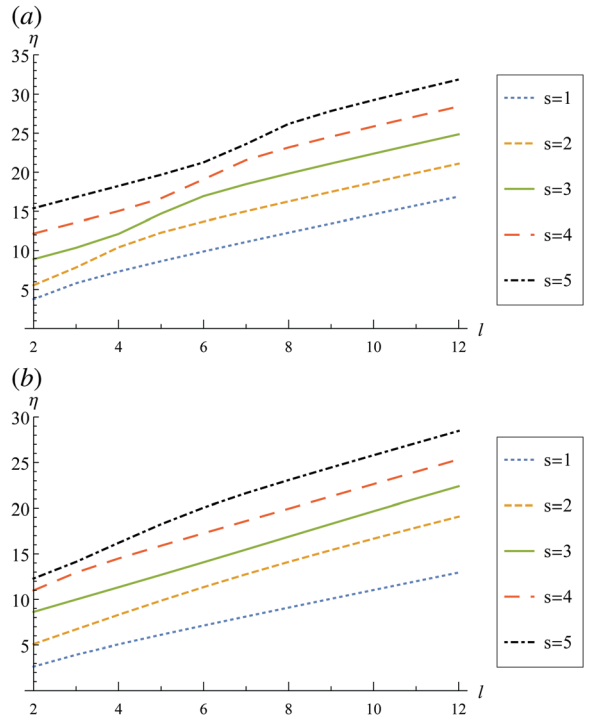

Fig. 2 Dispersion relationship. Frequency η against wavenumber l for (a) $\kappa = 0$, $\Sigma = 1$ and (b) $\kappa = 0.5$, $\Sigma = 0$ for the first five radial s modes.

3 Results

Frequencies η are readily computed from the nonlinear characteristic equations for the spheroidal (14) and torsional (12) modes, as they depend upon the polar wavenumber l, elastocapillary number Σ and compressibility number κ. Recall that frequencies are degenerate with respect to the azimuthal wavenumber m. For the spheroidal modes, the corresponding motions are determined from (13). We note that the torsional modes are independent of Σ, κ, because they do not change the shape of the sphere or have radial displacement u_r that is independent of the torsional potential T (Appendix A). Our interest is in shape change and the spheroidal modes of oscillation.

We begin this section by showing how the dispersion relationship, η against l, is effected by Σ and κ and contrast with the Rayleigh drop (1). For an incompressible gel drop $\kappa = 0$, we capture and describe the transition from elasticity-dominated to capillary-dominated motion for fixed l as it depends upon Σ. Asymptotic dispersion relationships are then derived in the elasticity-dominated $\Sigma \to 0$ and capillary-dominated $\Sigma \to \infty$ limits. Lastly, we discuss the unique $l = 0$ 'breathing' and $l = 1$ 'translational' modes and their dependence on Σ, κ.

3.1 Dispersion relationship

Recall that inviscid Rayleigh drops oscillate with a single frequency given by eqn (1) for each mode number l. For the elastic Rayleigh drop, the dispersion relationship is affected by the elastocapillary Σ and compressibility κ numbers. Fig. 2 plots the frequency η against wavenumber l for an (a) incompressible drop with finite surface tension ($\kappa = 0$, $\Sigma = 1$) and a (b) purely elastic compressible drop ($\kappa = 0.5$, $\Sigma = 0$). In contrast to the inviscid Rayleigh drop, Fig. 2 shows there are an infinite number of solutions for each wavenumber l that can be distinguished by a radial number s. For each s the dispersion curve is a monotonically increasing function of l but there are regions of faster and slower growth depending upon Σ and κ, which we discuss in detail next.

3.2 Frequency transition

Fig. 3(a) plots the $l = 4$ incompressible ($\kappa = 0$) frequency against the elastocapillary number Σ for the first five radial modes. As Σ increases, each frequency increases from a constant frequency plateau region to another plateau region of higher frequency. The low and high frequency regions correspond to elasticity-dominated and capillary-dominated behavior, respectively, and are separated by a sharp transition region characterized by a rapidly increasing capillary effect. Each frequency displays only one such transition and higher mode numbers transition at higher values of Σ. Similar behavior is seen for every spheroidal mode with $l \geq 2$.

To better understand the transition region, we plot the displacement field $\mathbf{u}$ in Fig. 3(b) for various Σ along the frequency curves. Note these are two-dimensional axisymmetric $m = 0$ deformation fields. Consider the $s = 1$ case, a single layer of recirculation vortices develops in the transition region $\Sigma = 0.3$ that becomes fully-developed in the capillary-dominated region $\Sigma = 10$. For the $s = 2$ mode, the single layer of recirculation vortices seen in the elasticity-dominated region

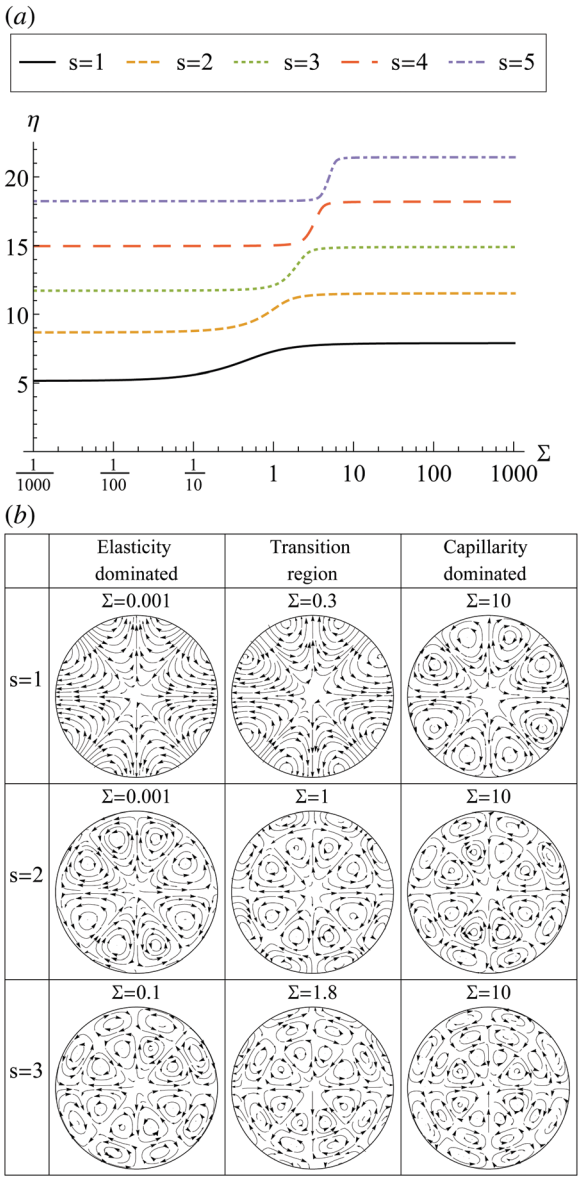

Fig. 3 Frequency transition for the $l = 4$ mode. (a) Frequency η against elastocapillary number Σ shows a transition from low frequency elasticity-dominated motion to high frequency capillarity-dominated motion for each radial s mode. (b) The deformation fields illustrate that in the transition region a set of vortices develop near the interface that eventually propagates into the bulk and becomes fully-developed in the capillary-dominated region.

$\Sigma = 0.001$ gets pushed to the center of the drop in the transition region $\Sigma = 1$ by the emergence of an additional layer of vortices that become fully-developed in the drop in the capillary-dominated region $\Sigma = 10$. Similar transitions occur for the $s = 3$ and higher order modes but at higher values of Σ. In general, the number of layers of vortices changes from $s - 1$ to s in the transition region and within each layer there are $2l$ individual vortices.

This behavior is robust and extends to all spheroidal modes. Recall the frequency is degenerate with respect to azimuthal wavenumber m, but the mode deformation fields are unique. For the axisymmetric modes $m = 0$, we observe the emergence of an additional layer of vortices in the transition region (*cf.* Fig. 3). We observe similar behavior in sectoral $l = m$ and tesseral $m \neq 0$ modes. Fig. 4 plots the surface shapes for the $s = 1$ (4,2), (6,3), (2,2) modes and associated deformation fields in the elasticity-dominated and capillary-dominated regions.

3.3 Asymptotic dispersion relations

It is straightforward to obtain closed-form dispersion relationships for the limiting cases $\Sigma \to 0$ and $\Sigma \to \infty$. These are the capillary-dominated and elasticity-dominated limits, respectively. For the capillary limit $\Sigma \to \infty$, we introduce the capillary time scale $t_c = (\rho R^3/\sigma)^{1/2}$, define $\zeta = \omega t_c$, and take the first order expansion of (17) about $\Sigma = \infty$ to give

$$\zeta^2 = l(l-1)(l+2) + (2l+1)(4l+3)\frac{1}{\Sigma}. \tag{16}$$

Note that we recover (1) in the limit $\Sigma \to \infty$, as expected. The scaling relationship with respect to Σ reproduces that reported by Chakrabarti and Chaudhury[23] for sessile drops. For the elasticity-dominated limit $\Sigma \to 0$, we note that (15) is already scaled with the elastic time scale $t_e = (\rho R^2/\mu)^{1/2}$ with $\eta = \omega t_e$ and we take the first order expansion about $\Sigma = 0$ to give

$$\eta^2 = \frac{2(l-1)(5+2l)(3+4l+2l^2)}{(2l+1)(3+4l)} + l(l-1)(l+2)(5+2l)\frac{\Sigma}{3+4l}. \tag{17}$$

Both (16) and (17) allow one to obtain quick frequency estimates without having to solve a nonlinear eqn (15).

3.4 The $l = 1$ 'translational' mode

For the inviscid Rayleigh drop, eqn (1) predicts zero-frequency $l = 0$ and $l = 1$ modes that correspond to volume conservation and translational invariance, respectively. However, for a soft elastic drop these produce non-trivial motions. The $l = 1$ 'translational' mode corresponds to a rigid translation of the sphere, as shown in Fig. 5(b), and is therefore independent of Σ (capillary effects) as there is no shape change associated with this motion. This can be easily seen by setting $l = 1$ in eqn (14). However, compressibility $\kappa \neq 0$ does affect the oscillation frequency for this mode. Fig. 5(a) plots the frequency η against compressibility number κ and shows complex behavior, whereby for fixed radial wavenumber s there are distinct plateau regions of constant frequency separated by transition regions where the frequency decreases with increasing κ. For reference, a typical deformation field for the $s = 1$ mode is shown in Fig. 5(c).

3.5 The $l = 0$ 'breathing' mode

The $l = 0$ 'breathing' mode produces a pure volumetric shape change in which the sphere uniformly compresses and expands during oscillation. These pure radial motions have zero curl, $\nabla \times \mathbf{u} = 0$ (6), and associated unknown constant A_{00} that can be determined from the normal stress balance (4) (the shear-free conditions are naturally satisfied). The resulting characteristic

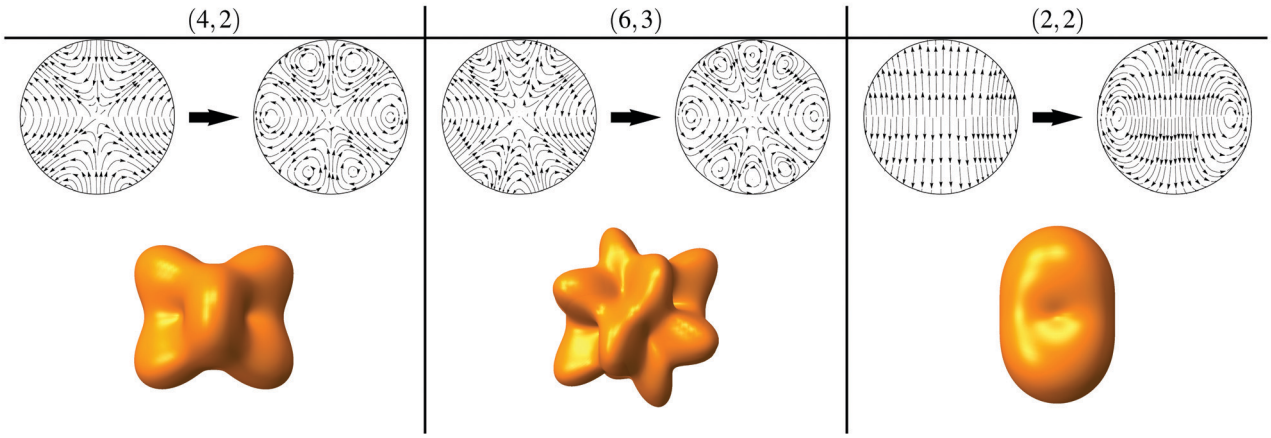

Fig. 4 Typical deformation fields for modes (l,m) illustrate the transition from elasticity- to capillary-dominated motion. Corresponding 3D mode shapes are shown in the bottom row. Note the deformation amplitude has been exaggerated for illustration purposes.

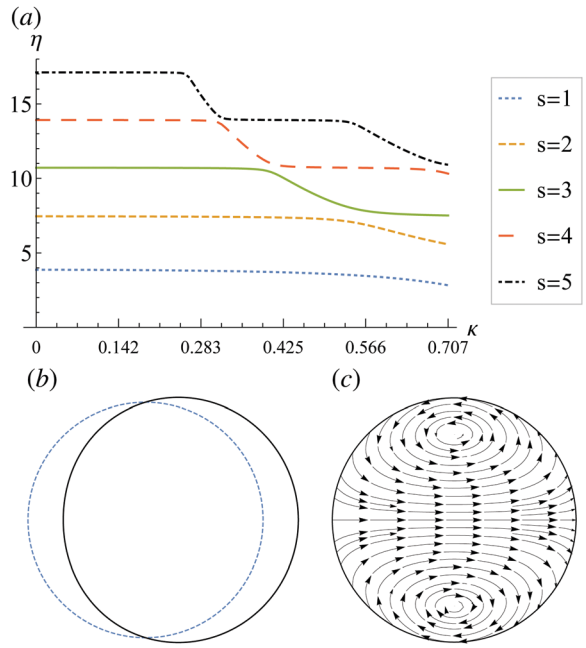

Fig. 5 'Translational' l = 1 mode. (a) Frequency η against compressibility number κ, (b) typical mode shape and (c) associated deformation field.

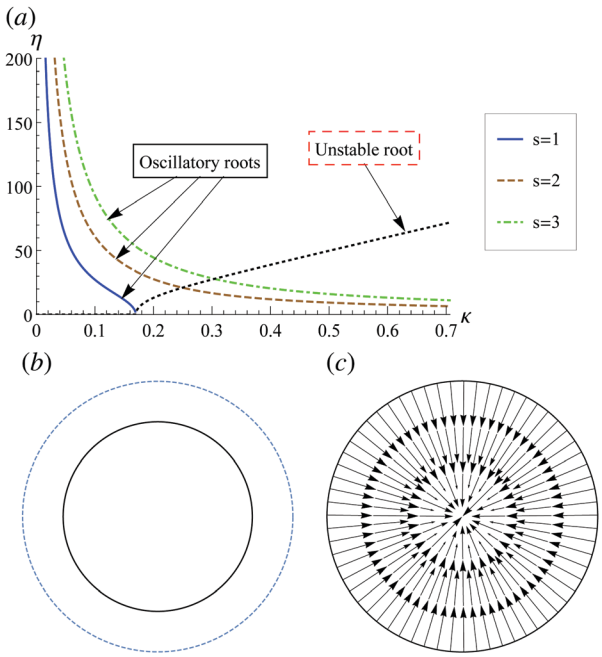

Fig. 6 'Breathing' l = 0 mode. (a) Frequency η against compressibility number κ displays oscillatory behavior, as well as an unstable root Re[$i\eta$] > 0 which bifurcates at a critical compressibility number κ* for Σ = 50. The unstable mode has (b) mode shape and (c) associated deformation field for κ = 0.2.

equation $T_{11}(\kappa\eta) = \Sigma Q_1(\kappa\eta)$ can be simplified into the following form,

$$\frac{\tan\kappa\eta}{\kappa\eta} = -\frac{4+2\Sigma}{\eta^2-(4+2\Sigma)} \tag{18}$$

For Σ = 0, the equation gives Love[45] solution for an elastic sphere which has infinite frequency when κ = 0. For compressible materials $\kappa > 0$, the frequency decreases with increasing compressibility. In addition to oscillatory motions, we find an unstable mode Re[$i\eta$] > 0 for finite elastocapillary number $\Sigma \neq 0$.

Fig. 6(a) plots the l = 0 frequency η against κ for finite elastocapillary number Σ = 50 and shows the oscillatory modes as well as the unstable mode bifurcating at a critical compressibility number κ*. After the bifurcation, the growth rate for the unstable mode continues to increase with κ. The mode shape and associated deformation field for the unstable mode are shown in Fig. 6(b) and (c), respectively. Here the radius of the drop decreases because surface tension tends to minimize the surface area of the drop. This leads to the collapse of the drop, as the elastic resistance is unable to counteract the increase in

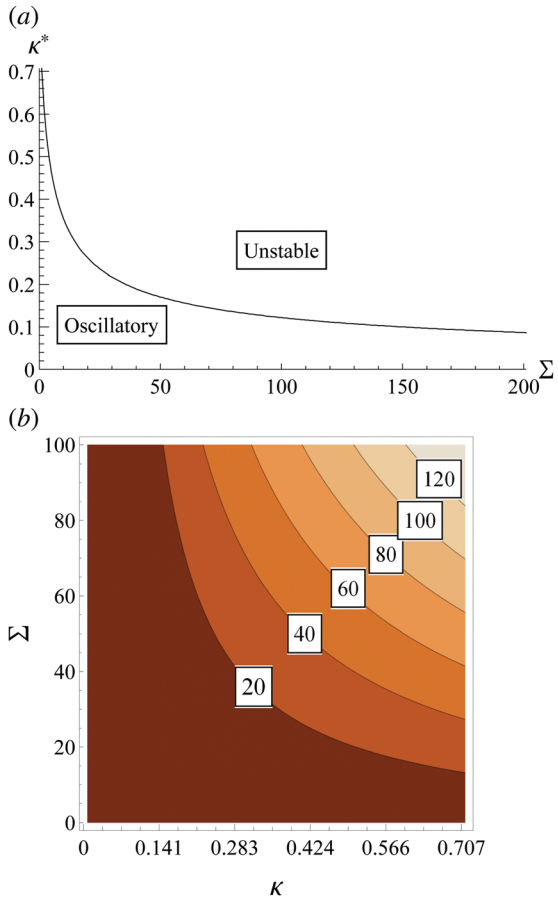

Fig. 7 (a) Stability diagram for the $l = 0$ mode plotting the critical compressibility number κ against elastocapillary number Σ separates regions of oscillatory (stable) and unstable behavior. (b) The growth rate Re[η] against compressibility number κ and elastocapillary number Σ for the unstable mode.

capillary pressure as the drop radius shrinks. This runaway process is typical of instabilities.

This instability is directly related to the compressibility of the soft solid. Recall that drops of incompressible liquid are stable due to the fluid pressure which resists surface tension. In contrast, bubbles have finite compressibility related to thermodynamic effects, but can similarly be stabilized provided the internal gas pressure is large enough. Soft compressible gel drops are most similar to bubbles since they also exhibit finite compressibility due to elastic effects. With regard to the elastic drop, surface tension exactly balances elasticity on the neutral stability curve shown in Fig. 7(a), which plots κ^* against Σ. This boundary separates region of instability from oscillatory (stable) behavior. For fixed κ, increasing Σ leads to instability. In the unstable region, the growth rate increases with both Σ and κ as shown in Fig. 7(b). That is, surface tension and compressibility drive the instability.

3.6 Torsional modes

As noted above, the torsional modes are decoupled from the spheroidal modes and satisfy the characteristic equation,

$$(l - 1)j_l(\eta) - \eta j_{l+1}(\eta) = 0. \quad (19)$$

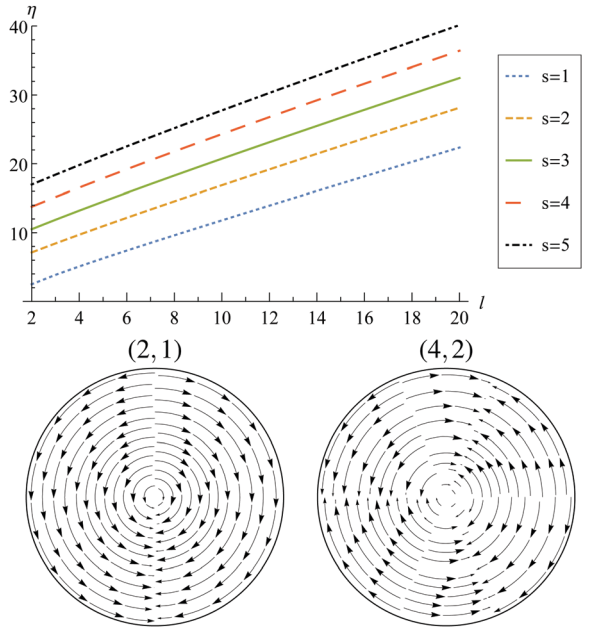

Fig. 8 Torsional modes. Dispersion relationship plotting frequency η against wavenumber l (left) and typical deformation fields for the $s = 1$ (2,1) and (4,2) modes (right).

These motions do not change the shape of the sphere and, as such, are independent of compressibility κ and capillary Σ effects. This is evident by the absence of the potential function T in the radial displacement u_r (Appendix A). Fig. 8 plots the dispersion relationship η against l for these modes with sample deformation fields.

4 Conclusion

We have developed a model that describes the oscillations of a soft spherical gel drop, which behaves as a linear elastic solid with non-trivial surface tension. In contrast to the inviscid Rayleigh drop, there are an infinity of radial modes s for each polar wavenumber l and the dispersion relationship for each depends upon the elastocapillary Σ and compressibility κ numbers. The nonlinear characteristic equation is independent of the azimuthal wavenumber m and admits two classes of solutions; (i) spheroidal and (ii) torsional modes. The spheroidal modes are associated with droplet shape change, while the torsional modes are not and therefore independent of Σ. For the spheroidal modes, we show a transition from elasticity-dominated to capillary-dominated motion for increasing Σ and this transition is accompanied by the emergence of a set of recirculation vortices at the drop interface that propagates into the bulk in the capillary region. Two asymptotic dispersion relations are developed for low and high Σ that recover existing asymptotic limits, such as the Rayleigh drop. Lastly, we discuss the special $l = 0$ breathing and $l = 1$ translational modes and their unique dependence on Σ and κ. Notably, we have documented an unstable $l = 0$ mode that leads to drop collapse and computed the associated neutral stability curve that reflects a

balance between surface tension and compressibility. For an incompressible material, the drop is stable consistent with well-known results for incompressible liquids.

Recent interest in bioprinting applications make our results particularly timely. Specifically, bioprinting uses the same principles of inkjet printing, such as capillary breakup, but adapted for biologically-compatible gels, such as agarose or alginate. These gels are typically soft (small, but finite elasticity) and have dynamics that are affected by both elasticity and surface tension. Hence, the Rayleigh drop dispersion relationship (1) can be expected to be of limited utility in predicting the complex dynamics. Our results illustrate elastocapillary effects in a dynamic system and contribute to this emerging field. In fact, our model predictions could be used as a diagnostic tool to measure the surface tension of soft gels, similar to immiscible liquid drops[46] or free drops in microgravity.[47] This technique has been recently applied to hydrogels using mechanically-excited planar Faraday waves[24] and the oscillations of a hemispherical drop excited by white noise.[48] For a drop with a complex viscoelastic rheology, the shear modulus $\mu = \mu' + i\mu''$ has a real part corresponding to the storage modulus (elasticity) and an imaginary part corresponding to the loss modulus (proportional to viscosity) and these quantities often depend upon the frequency $\mu'(\omega)$, $\mu''(\omega)$. For such materials, the governing equations depend upon the rheology and become more complex to solve since the frequency appears in the stress–strain relaxation equations; each problem would have to be treated independently.

To model the dynamics that incorporates a complex rheology one would need to consider a frequency dependent complex shear modulus with real and imaginary parts corresponding to stored and lost energy due to strain, replacing $\mu = \mu' + i\mu''$. Here, μ'' will characterize the energy lost during the oscillation due to viscous damping.

Future directions include experimental realization of our model predictions, adapting our model to predict other fundamental capillary instabilities in soft materials (Plateau–Rayleigh, Rayleigh–Taylor), extending our basic model to include viscoelastic effects for materials with complex rheology, and adapting the model to account for wetting effects[49,50] in sessile gel droplets. For example, recent work by Chakrabarti and Chaudhury[23] on sessile hydrogel drops has shown that higher order modes cannot be excited due to viscous effects; *i.e.* the resonance peak disappears in a frequency response diagram for those modes, thus highlighting the role of elasticity and viscosity in drop oscillations. This is also seen for sessile drops of Newtonian fluids and it is well-known that higher order modes damp out more quickly.[51] Therefore, new models of drop oscillations in complex fluids should include both elasticity and viscosity.

Conflicts of interest

There are no conflicts to declare.

Appendix

A Displacement components

The components of the displacement field $\mathbf{u} = (u_r, u_\theta, u_z)$ are given by

$$\begin{aligned} u_r &= \frac{1}{r}[A_{lm}(lj_l(\alpha r) - \alpha r j_{l+1}(\alpha r)) \\ &\quad + C_{lm} l(l+1) j_l(\beta r)]\, Y_l^m(\theta, \varphi) \end{aligned} \tag{20}$$

$$\begin{aligned} u_\theta &= \frac{1}{r}[A_{lm} j_l(\alpha r) + C_{lm}((l+1) j_l(\beta r) - \beta r j_{l+1}(\beta r))] \\ &\quad \times \left(m \cot\theta\, Y_l^m(\theta, \varphi) + \sqrt{(l-m)(l+m+1)}\, \mathrm{e}^{-i\varphi}\, Y_l^{m+1}(\theta, \varphi) \right) \\ &\quad + \frac{i B_{lm} m j_l(\beta r)}{\sin\theta} Y_l^m(\theta, \varphi) \end{aligned} \tag{21}$$

$$\begin{aligned} u_\varphi &= \frac{im}{r \sin\theta}[A_{lm} j_l(\alpha r) + C_{lm}((l+1) j_l(\beta r) \\ &\quad - \beta r j_{l+1}(\beta r))]\, Y_l^m(\theta, \varphi) - \frac{1}{r} B_{lm} j_l(\beta r) \left(m \cot\theta\, Y_l^m(\theta, \varphi) \right. \\ &\quad \left. + \sqrt{(l-m)(l+m+1)}\, \mathrm{e}^{-i\varphi}\, Y_l^{m+1}(\theta, \varphi) \right) \end{aligned} \tag{22}$$

Acknowledgements

JBB acknowledges support from NSF Grant CBET-1750208.

References

1 L. Rayleigh, *Proc. R. Soc. London*, 1879, **29**, 71–97.
2 T. MacRobert, *Spherical Harmonics*, Pergamon, New York, NY, 1967.
3 J. Kim, *Int. J. Heat Fluid Flow*, 2007, **28**, 753–767.
4 P. Calvert, *Chem. Mater.*, 2001, **13**, 3299–3305.
5 O. A. Basaran, H. Gao and P. P. Bhat, *Annu. Rev. Fluid Mech.*, 2013, **45**, 85–113.
6 B. Derby, *Science*, 2012, **338**, 921–926.
7 R. Landers, U. Hübner, R. Schmelzeisen and R. Mülhaupt, *Biomaterials*, 2002, **23**, 4437–4447.
8 P. Zarrintaj, S. Manouchehri, Z. Ahmadi, M. R. Saeb, A. M. Urbanska, D. L. Kaplan and M. Mozafari, *Carbohydr. Polym.*, 2018, **87**, 66–84.
9 J. Nase, A. Lindner and C. Creton, *Phys. Rev. Lett.*, 2008, **101**, 074503.
10 R. Okamoto, E. Clayton and P. Bayly, *Phys. Med. Biol.*, 2011, **56**, 6379.
11 G. H. McKinley, *Dimensionless groups for understanding free surface flows of complex fluids*, 2005, http://web.mit.edu/nnf/publications/GHM78.pdf.
12 H. Barnes, *A Handbook of Elementary Rheology*, University of Wales, Institute of Non-Newtonian Fluid Mechanics, 2000.

13 J. Wang, D. D. Joseph and T. Funada, *J. Nonnewton. Fluid Mech.*, 2005, **129**, 106–116.
14 R. W. Style, A. Jagota, C.-Y. Hui and E. R. Dufresne, *Annu. Rev. Condens. Matter Phys.*, 2017, **8**, 99–118.
15 B. Andreotti and J. H. Snoeijer, *Annu. Rev. Fluid Mech.*, 2020, **52**, DOI: 10.1146/annurev-fluid-010719-060147.
16 J. Bico, É. Reyssat and B. Roman, *Annu. Rev. Fluid Mech.*, 2018, **50**, 629–659.
17 R. Shuttleworth, *Proc. Phys. Soc. Sect. A*, 1950, **63**, 444.
18 F. Monroy and D. Langevin, *Phys. Rev. Lett.*, 1998, **81**, 3167.
19 J. Harden, H. Pleiner and P. Pincus, *J. Chem. Phys.*, 1991, **94**, 5208–5221.
20 S. Mora, T. Phou, J.-M. Fromental, L. M. Pismen and Y. Pomeau, *Phys. Rev. Lett.*, 2010, **105**, 214301.
21 S. Mora, C. Maurini, T. Phou, J.-M. Fromental, B. Audoly and Y. Pomeau, *Phys. Rev. Lett.*, 2013, **111**, 114301.
22 S. Mora, T. Phou, J.-M. Fromental and Y. Pomeau, *Phys. Rev. Lett.*, 2014, **113**, 178301.
23 A. Chakrabarti and M. K. Chaudhury, *Extreme Mech. Lett.*, 2014, **1**, 47–53.
24 X. Shao, J. Saylor and J. B. Bostwick, *Soft Matter*, 2018, **14**, 7347–7353.
25 M. Tokita and K. Hikichi, *Phys. Rev. A: At., Mol., Opt. Phys.*, 1987, **35**, 4329.
26 C. Storm, J. J. Pastore, F. C. MacKintosh, T. C. Lubensky and P. A. Janmey, *Nature*, 2005, **435**, 191.
27 A. V. Dobrynin and J.-M. Y. Carrillo, *Macromolecules*, 2010, **44**, 140–146.
28 M. Jaspers, M. Dennison, M. F. Mabesoone, F. C. MacKintosh, A. E. Rowan and P. H. Kouwer, *Nat. Commun.*, 2014, **5**, 5808.
29 K. A. Whitaker, Z. Varga, L. C. Hsiao, M. J. Solomon, J. W. Swan and E. M. Furst, *Nat. Commun.*, 2019, **10**, 2237.
30 A. C. Eringen and E. S. Suhubi, *Elastodynamics, Volume II, Linear Theory*, Academic Press, 1975.
31 T. Young, *Philos. Trans. R. Soc. London*, 1805, **95**, 65–87.
32 R. Laplace, *An essay on the cohesion of fluids*, Coureier, Paris, 1806.
33 P.-G. de Gennes, F. Brochard-Wyart and D. Quéré, *Capillarity and wetting phenomena: drops, bubbles, pearls, waves*, Springer Science & Business Media, 2013.
34 L. Rayleigh, *Proc. London Math. Soc.*, 1885, **1**, 4–11.
35 A. E. H. Love, *Some problems of geodynamics*, Cambridge University Press, 2015.
36 J. Pujol, *Elastic wave propagation and generation in seismology*, Cambridge University Press, 2003.
37 H. Portales, L. Saviot, E. Duval, M. Fujii, S. Hayashi, N. Del Fatti and F. Vallée, *J. Chem. Phys.*, 2001, **115**, 3444–3447.
38 L. Saviot and D. B. Murray, *Phys. Rev. B: Condens. Matter Mater. Phys.*, 2005, **72**, 205433.
39 P. M. Shearer, *Introduction to seismology*, Cambridge University Press, 2009.
40 K. F. Riley, M. P. Hobson and S. J. Bence, *Mathematical methods for physics and engineering: a comprehensive guide*, Cambridge University Press, 2006.
41 H. Lamb, *Proc. London Math. Soc.*, 1881, **1**, 189–212.
42 H. Lamb, *Hydrodynamics*, Cambridge University Press, 1932.
43 J. B. Bostwick and K. E. Daniels, *Phys. Rev. E: Stat., Nonlinear, Soft Matter Phys.*, 2013, **88**, 042410.
44 M. Grzelka, J. B. Bostwick and K. E. Daniels, *Soft Matter*, 2017, **13**, 2962–2966.
45 A. E. H. Love, *A treatise on the mathematical theory of elasticity*, Dover, 1944.
46 E. Trinh and T. Wang, *J. Fluid Mech.*, 1982, **122**, 315–338.
47 T. Wang, A. Anilkumar and C. Lee, *J. Fluid Mech.*, 1996, **308**, 1–14.
48 A. Chakrabarti and M. K. Chaudhury, *Langmuir*, 2013, **29**, 6926–6935.
49 J. Bostwick and P. Steen, *J. Fluid Mech.*, 2014, **760**, 5–38.
50 P. H. Steen, C.-T. Chang and J. B. Bostwick, *Proc. Natl. Acad. Sci. U. S. A.*, 2019, **116**, 4849–4854.
51 J. B. Bostwick and P. H. Steen, *Soft Matter*, 2016, **12**, 8919–8926.

